Published in final edited form as:
J Phys Chem C Nanomater Interfaces. 2012 November 15; 116(45): 24224–24232. doi:10.1021/jp3057527.

Bimetallic Nanoshells for Metal – Enhanced Fluorescence with Broad Band Fluorophores

Jian Zhang[1,*], **Yi Fu**[1], and **Farhad Mahdavi**[2]

[1]Center for Fluorescence Spectroscopy, University of Maryland School of Medicine, Department of Biochemistry and Molecular Biology, 725 West Lombard Street, Baltimore, MD 21201

[2]Electrical and Computer Engineering Department, University of Utah, 50 S. Central Campus Dr., Salt Lake City, UT 84112

Abstract

In this article, we reported the near-field interactions between the $Ru(bpy)_3^{2+}$ complexes and plasmon resonances from the bimetallic nanoshells. The metallic nanoshells were fabricated on 20 nm silica spheres as cores by depositing 10 nm monometallic or bimetallic shells. There were approx. 15 $Ru(bpy)_3^{2+}$ complexes in the silica core. The metal shells were constituted of silver or/and gold. The bimetallic shells could be generated in homogeneous or heterogeneous geometries. The homogeneous bimetallic shells contained 10 nm silver-gold alloys. The heterogeneous bimetallic shells contained successive 5 nm gold and 5 nm silver shells, or alternatively, 5 nm silver and 5 nm gold shells. Optical properties of metal nanoshells were studied on both the ensemble spectra and single nanoparticle imaging measurements. The heterogeneous bimetallic shells were found to have a large scale of metal-enhanced emission relative to the monometallic or homogeneous bimetallic shells. It is because the heterogeneous bimetallic shells may display split dual plasmon resonances which can interact with the excitation and emission bands of the $Ru(bpy)_3^{2+}$ complexes in the silica cores leading to more efficient near-field interactions. The prediction can be demonstrated by the lifetimes. Therefore, it is suggested that both the compositions and geometries of the metal shells can influence the interactions with the fluorophores in the cores. This observation also offers us an opportunity for developing plasmon-based fluorescence metal nanoparticles as novel nanoparticle imaging agents which have high performances in fluorescence cell or tissue imaging.

Keywords

fluorescence; bimetallic nanoshell; plasmon resonance; $Ru(bpy)_3^{2+}$ complexes; optical properties of single nanoparticle; time-resolved confocal microscope; and near-field interaction

Introduction

Fluorescence metal nanoparticles recently are attracting considerable research interest because of their highly favorable optical properties and great potential in clinical and biomedical applications [1,2]. Relative to free fluorophores, these metal nanoparticles can exhibit increased emission signals up to 10 - 10^3 fold due to the near-field interactions between the fluorophores and metal nanoparticles [3,4]. Fundamentally, when induced by an incident light, a metal nanoparticle that has a subwavelength size can bring up collective oscillations of free electrons on its surface resulting in an enhanced local electromagnetic field nearby [5,6]. This local field is also regarded to be due to plasmon resonance from the

Information for contact author: jianzhang@umaryland.edu, Tel: 410-706-7500, Fax: 410-706-8409.

metal nanoparticle. When a fluorophore is localized near the metal nanoparticle within a near-field distance, the fluorophore can be excited by the local field, additionally, and the emission from the fluorophore is efficiently coupled with the plasmon resonance from the metal nanoparticle leading to a significant increased fluorescence. This near-field interaction is also considered to occur at both the excitation and emission processes of the fluorophore. The increased emission by the near-field interaction hence is thought to compose of two components: increased quantum yield of the fluorophore and simultaneous energy emission of the plasmon resonance from the metal nanoparticle at the same wavelength [5,6]. The near-filed interaction can be interpreted initially using a modified Mie theory [7,8]. The extinction properties of metal nanoparticles can be expressed by a combination of both absorption (C_A) and scattering (C_S) factors,

$$C_E = C_A + C_s = k_1 \mathrm{Im}(\alpha) + \frac{k_1^4}{6\pi}|\alpha|^2 \quad (1)$$

where $k_1 = 2\pi n_1/\lambda_0$ is the wavevector of the incident light in medium 1 and α is the polarizability of the sphere of radius r,

$$\alpha = 4\pi r^3(\varepsilon_m - \varepsilon_1)/(\varepsilon_m + 2\varepsilon_1) \quad (2)$$

and ε_m is the complex dielectric constant of metal. The first term represents the cross section due to absorption and the second term represents the cross section due to scattering. The absorption component may contribute to the local fields. We expect the absorption factor C_A to cause quenching for a fluorophore and the factor of scattering C_S to cause enhancement. The quenching term increases as the r^3 factor, and the enhancement term increases as the r^6 factor. Hence, a small metal nanoparticle can quench fluorescence because the absorption dominates over the scattering. In contrast, a large metal nanoparticle can enhance fluorescence because the scattering component becomes the dominant factor over the absorption component.

The near-field interactions between the fluorophores and metal nanoparticles are suggested to rely on some factors from both the metal nanoparticles and fluorophores as well as other factors such as distances between them and environments of media [9–11]. For instance, the metal nanoparticles may be fabricated with different metal species, particle sizes, and shapes, etc, and thus, have different local fields. The fluorophores may be selected with different excitation and emission wavelengths for their different interaction in the local fields. Since the near-field interactions are thought to occur through spaces, the chemical structures of fluorophores are not expected to be a factor as large as others unless the fluorophores have chemical interactions with the metal nanoparticles. The distance from the fluorophore to the metal nanoparticle is also regarded as an important factor since an excited fluorophore can be quenched when it is localized in proximate to the metal surface and if the distance is beyond near-field there is not interaction between the fluorophore and metal. Our experiment data also demonstrate that the optimal distance for the meta-enhanced fluorescence is ca. 10 nm from the fluorophore to the metal nanoparticle. In fact, the factor of optimal distance is found to rely on the geometry of metal nanostructure. In this research, we are particularly interested in the metal core/nanoshell structures [12–14] because according to theoretical calculations, the metal nanoshells have uniform electric fields in the cores [15,16], and therefore, the fluorophores within the cores of metal shells can equally and efficiently interact with the plasmon resonances. In the metal shells, there is no significant distance factor for the near-field interactions. In addition, the near-field interactions can increase a radiative rates of fluorophores leading to a decrease of lifetime

which may allow less time for photochemistry of fluorophores while in the excited states leading to more excitation-emission cycles prior to its complete photobleaching [5,6]. As a result, the photostability of fluorophores in the metal nanoshells can be significantly increased. This feature can increase the observation time for fluorescence cell imaging or single-molecule detection when the metal nanoshells are used as imaging agents.

In our previous works, we reported the fabrications of metal nanoshells only with monometallic component of silver or gold [17–19]. Different fluorophores were also selected to encapsulated within the cores of the metallic shells to investigate the near-field interactions between them [19] However, we also notice that the monometallic shells display only a single plasmon band, and thus, they cannot interact efficiently with the fluorophores at both the excitation and emission processes of the fluorophores especially when the fluorophores have a large Stokes shift [20]. Consequently, the fluorophore-contained metal shells cannot display optimally enhanced fluorescence. Therefore, there is a basic need to develop the metal shells with dual or multiple plasmon bands that can consist with the excitation and emission bands of the fluorophores.

Aside of mono-component of metal, the metal nanoshells can be fabricated with two or more components of noble metals [21–25]. These multimetallic nanoshells can display unique optical properties including multiple plasmon bands when they are fabricated with distinctly heterogeneous geometries. In this work, the bimetallic nanoshells which contain the distinctly separated metal layers were fabricated to optimize their spectral properties. The $Ru(bpy)_3^{2+}$ complexes that have significantly separated absorbance and emission bands were encapsulated in the silica cores of the bimetallic shells. We expect that the two plasmon bands from the bimetallic shells can respectively interact with the excitation and emission bands of the $Ru(bpy)_3^{2+}$ complexes in the near-field range [28,29]. The optical properties of these metal nanoshells including the emission intensity and lifetime were determined on the ensemble spectra and single nanoparticle imaging. Moreover, the bimetallic shells were also fabricated in a homogeneous alloy geometry which could exhibit only a single plasmon band. The $Ru(bpy)_3^{2+}$ complexes were encapsulated in the cores and the emission properties from the homogeneous bimetallic shells were measured as the control [30,31]. Influences from the metal compositions and geometries to the near-field interaction were studied in this report.

Experimental Section

All reagents and spectroscopic grade solvents were used as received from Fisher or Sigma/Aldrich. Monodispersed silica spheres (average diameter = 20 nm) were from Sigma/Aldrich. Nanopure water (>18.0 MΩ cm^{-1}) purified using Millipore Milli-Q gradient system, was used in all experiments.

Preparation of Ru(II) complex-doped silica spheres

We first aminated the 20 nm silica spheres for their binding with the metal shells. In brief, 0.1 g of monodispersed silica spheres were dispersed in 50 mL ethanol followed by adding 50 μL 3-aminopropyltrimethoxy silane. The solution was continuously stirred for 5 h [17,18]. The aminated silica spheres were recovered from the reaction solution by centrifugation and washed completely with ethanol and water, respectively. The aminated silica spheres were then co-dispersed with 1.0 mg of tris(2,2′-bipyridyl)dichlororuthenium(II) hexahydrate (abbreviated as $Ru(bpy)_3^{2+}$ complexes) in 10 mL water solution. The solution was continuously stirred for 24 h. The mixture was centrifuged to remove the suspension, and the residual solid of silica spheres was washed thoroughly with water. The recovered silica spheres were found to become orange color indicating the $Ru(bpy)_3^{2+}$ complexes were encapsulated in the silica spheres through the

physical absorptions. According to the emission spectral change from the $Ru(bpy)_3^{2+}$ complex in the reaction solution prior to and after the absorptions, the consuming amount of $Ru(bpy)_3^{2+}$ complex in the solution could be estimated [17–19], and therefore, the numbers of doped $Ru(bpy)_3^{2+}$ complexes in the silica spheres could be estimate. The silica spheres were redispersed in 10 mL water with a concentration of ca. 3×10^{-6} M. These silica spheres in solution were used as the cores for depositing the monometallic or bimetallic shells on their external surfaces.

Deposition of monometallic nanoshells on silica spheres

Many strategies can be used to fabricate the monometallic shells on the silica spheres [32,33]. In this work, a wet chemical reduction method was employed to deposit the metal shells on the silica spheres. In the reaction, the silver or/and gold salts in solution were reduced to deposited as metal thin layers on the silica spheres [18,19]. The citrate salt was used as reduction reagent. The monometallic shells were first fabricated (Scheme 1). For the silver shells, the 4 nm silver nanoparticles with the citrate coating were generated by a chemical reduction of $AgNO_3$ using ascorbic acid as reduction agent at first [34]. These silver nanoparticles were then codispersed in aqueous solution (ca. 1×10^{-5} M) with the $Ru(bpy)_3^{2+}$-doped silica spheres (2.7×10^{-7} M) at pH = 7.4. The solution was stirred for 4 h. It was shown that the silver nanoparticles were bound on the silica spheres precipitating from solution. The binding between the silver nanoparticles and silica spheres should occur via interactions of amino moieties on the silica with the metal. These bound metal nanoparticles could be used as seeds for smooth growths of metal shells on the silica spheres. The supernatant was removed from solution by centrifugation. The recovered silica-silver complexes were redispersed in 10 mL water (concentration = ca. 1×10^{-7} M) with the silver nitrate (1×10^{-4} M) and citrate (2×10^{-3} M). The solution was stirred for 2 h at 60°C, and consequently, the silver shells were observed to form on the silica spheres and precipitate from solution. The formed silver shells were recovered from solution by centrifugation and washed with water. Alternatively, in the similar strategy, the monometallic gold shells were also fabricated. In this case, these monometallic shells are represented to be silica/Ag for the silver shells or silica/Au for the gold shells, respectively.

Deposition of bimetallic nanoshells on silica spheres

Aside of the monometallic shells, the bimetallic shells were also fabricated in the wet chemical reduction method. These bimetallic shells were designed to have two configurations: heterogeneous and homogeneous geometries (Scheme 1). Heterogeneous bimetallic shells were made in a successive reduction method whereas homogeneous bimetallic shells were in a simultaneous reduction method [28]. For the heterogeneous bimetallic shells, we could fabricate them in either silica/Ag/Au geometry or silica/Au/Ag geometry. For the silica/Ag/Au geometry, in the strategy of monometallic shell fabrication, the silica-metal complexes were dispersed in 10 mL water (ca. 1×10^{-7} M) with the silver nitrate (3×10^{-5} M) and citrate (6×10^{-4} M). The solution was stirred for 2 h at 60°C to form the monometallic silver shells. The silver shells were recovered from solution by centrifugation and then washed with water. The recovered silver shells were then dispersed in 10 mL water (ca. 1×10^{-7} M) with the gold(III) chloride (7×10^{-5} M) and citrate (2×10^{-3} M) for a successive reduction of gold salt to form gold shells on the silver shells. The formed heterogeneous silica/Ag/Au shells were treated as described previously. Alternatively, in the same strategy, the silica/Au/Ag shells were also fabricated by first reduction of gold salt followed by reduction of silver salt.

Homogeneous alloy shells of silver and gold could be fabricated by simultaneous reduction of gold and silver salts in solution [30,31. Typically, the silica-silver complexes were co-dispersed in 10 mL water (ca. 1×10^{-7} M) with the silver nitrate (5×10^{-5} M) and gold(III)

chloride (5×10^{-5} M) at a molar ratio of 1/1. Citrate salt (1×10^{-3} M) was then added in solution followed by a continuous stirring for 2 h at 60°C. The homogeneous alloy shells were observed toform on the silica spheres and the formed metal shells were precipitated from solution. They were recovered from solution by centrifugation and washed with water.

To improve the chemical stability, all monometallic or bimetallic metal shells were dispersed in aqueous solution with 10 mM N-(2-mercapto-propionyl)glycine (abbreviated as tiopronin) [35] to form assembled tiopronin monolayers on the metal shells. The tiopronin monolayer-coated metal shells were observed to exhibit good chemical and photo stability in solution.

Spectra measurements

Ensemble absorption spectra were monitored with a Hewlett Packard 8453 spectrophotometer. Fluorescence spectra were recorded with a Cary Eclipse Fluorescence Spectrophotometer.

The emission signals of single metal shells were recorded on a time-resolved scanning confocal microscope (MicroTime 200, PicoQuant) as emission intensity and lifetime imaging. The imaging system consists of an inverted confocal microscope coupled to a high-sensitivity detection setup. A single mode pulsed laser diode (470 nm, 100 ps, 10 MHz) was used as the excitation source. An oil immersion objective (Olympus, 100×, 1.3 NA) was used to focus the laser beam on the sample and to collect the emission from the sample. The emission signals passed a dichroic mirror and focused onto a 75-μm pinhole for a spatial filtering and were recorded on a single photon avalanche diode (SPAD) (SPCM-AQR-14, Perkin-Elmer Inc.). A band filter of 610/70 nm was used to eliminate the residual emission signals. The data were collected with a TimeHarp 200 board and stored in time-tagged time-resolved mode (TTTR).

For the TEM measurements, the nanoparticle samples were diluted to nano-molar concentrations followed by casting onto the copper grids (200 mesh) with standard carbon-coated Formvar films (200–300 Å). The samples were dried in air. TEM images were taken with a side-entry Philips electron microscope at 120 keV. The distributions of nanoparticle sizes were analyzed with Scion Image Beta Release 2 on the base on at least 200 images.

Theoretical computation

Plasmon resonance bands of metal shells were calculated using Finite Element Method (FEM) simulation as the main theoretical analysis method for estimating the electromagnetic fields near the metal shells [36,37]. *Mie theory can be used for a multi-shell of metal nanoparticle if the extinction/scattering cross-section and field distribution are regard to be ideal in the shells. However, if there is any dipole embedded within the shell structure to simulate the emission of a fluorophore, the dipole may break the spherical symmetry of field inside of the core, and as a result, Mie theory can no longer be used. We are interested in the near-filed interactions of fluorophores with the metal plasmon resonances. The factors from fluorophores often need to be considered. Thus, in this case, Comsol was used to solve Maxwell equations.* The simulations were done using a commercial software Comsol® Multiphysics version 3.4. Multiphysics were in the beginning a PDE tool box for Mathworks MATLAB® which later became an add-on application with the name FEMLAB®. The program is now independent but still compatible with MATLAB®. It is a multipurpose FEM program which can be used for many different types of simulations within a wide range of areas in physics. Typically, we used scattering formalization which basically determines the scattering part of the field. Simulation environment was a metal shell with a 40 nm diameter containing a silica core with a 20 nm diameter inside. The power was

measured on the top hemisphere where the incident wave was X polarized and traveling in the positive Z direction. For the optical properties of metals we used a lookup table with Piecewise cubic interpolation, based on Handbook of Optical Constants of Solids by Edward Palik. For calculating the extinction factor we used the logarithm of the measured power of wave without the metal nanoparticle divided by the power of the wave with the metal nanoparticle.

Results and Discussion

Prior to the fabrications of metal shells on the silica spheres, we first aminated the silica spheres on their external surfaces using 3-aminopropyltrimethoxy silane in ethanol solution, which could increase the binding of the metal shells on the silica spheres [17–19]. The $Ru(bpy)_3^{2+}$ complexes were followed by absorbing from the solution into the silica spheres through the physical interactions. According to the change of the emission spectrum from the $Ru(bpy)_3^{2+}$ complex in solution before and after the absorption, the consuming amount of $Ru(bpy)_3^{2+}$ complex in solution could be estimated [17–19]. On the basis of this amount, we could infer an average number of the $Ru(bpy)_3^{2+}$ complex in each silica sphere that is 15 in this case. In contrast to the free $Ru(bpy)_3^{2+}$ complexes in aqueous solution that displayed an absorbance maximum at 448 nm (Figure 1), the $Ru(bpy)_3^{2+}$-doped silica spheres could not display a well-defined absorption spectrum because of their strong light scattering even though they became orange color due to the doped complexes. Upon the excitation at 450 nm, the $Ru(bpy)_3^{2+}$-doped silica spheres displayed an emission maximum at 598 nm (Figure 4a), 15 nm shift to blue from the free $Ru(bpy)_3^{2+}$ complexes. The emission band from the $Ru(bpy)_3^{2+}$-doped silica spheres also became broader relative to that of the free $Ru(bpy)_3^{2+}$ complexes which was due to the restrictions of movements for the localized $Ru(bpy)_3^{2+}$ complexes and the change of their microenvironments in the silica spheres.

To smoothly grow the metal shells on the silica spheres, the silica spheres were first bound by the small metal nanoparticles on their surfaces as seeds. These small silver or gold nanoparticles were created with the citrate monolayers as stabilizers on the external surfaces and had an average diameter of 4 nm [32,33]. Briefly, these small metal nanoparticles were codispersed with the $Ru(bpy)_3^{2+}$-doped silica spheres in solution to form the silica-metal complexes. In the reaction, there was a significant color change for the dispersed silica spheres from orange to deep yellow (silver case) or deep red (gold case), confirming combination of the metal nanoparticles with the silica spheres. The combinations could be also demonstrated on the TEM images (not shown). These silica-metal complexes were used to grow the metallic shells.

Typically, the metallic shells were fabricated in a wet chemical reduction method. The citrate was used as reduction agent [17–19]. We first fabricated the monometallic silver or gold shells. The formed metal shells on the silica spheres could be distinctly outlined with the TEM images (Figure 2). Controlling the amount of metal salt in the reaction, the thickness of metal shells could be defined well. It was shown that on the TEM images, the formed monometallic nanoshells had an average diameter of ca. 40 nm (Figure 2b and c). On the other hand, the silica spheres were shown to have an average diameter of ca. 20 nm (Figure 2a). Consequently, the metal shells on the silica spheres were estimated to have an average thickness of ca. 10 nm. Counting at least 200 TEM images, the size distributions of silica spheres and metal shells were analyzed with Scion Image Beta Release 2, showing that the metal shells appear to be approximately homogeneous in which at least 80% of them are distributed in a range of 40 ± 10 nm. Thus, we feel that the metal shells fabricated in this research can be used for studying the near-field interactions with the fluorophores in the silica cores.

Aside of the monometallic shells, the metallic shells were fabricated in the bimetallic components for investigating their unique plasmon resonances and interactions with the $Ru(bpy)_3^{2+}$ complexes in the cores of metal shells. Both the simultaneous and successive reduction methods were employed to fabricate the bimetallic shells that had different geometries [28–31]. In the simultaneous reduction method, the silver and gold salts were reduced simultaneously from solution leading to their depositing on the silica spheres as homogeneous alloy shells. In the reaction, the gold and silver salts were codissolved in aqueous solution at the molar ratio of 1/1 and then the silica-silver complexes were added into the solution. The citrate was used to reduce the gold and silver salts from the reaction [30,31]. Although the silver and gold salts were known to have different reduction speeds, consequently, both the gold and silver were observed to deposit on the silica spheres and the formed metal shells were in approximately homogeneous alloy shells. Like in the reaction of the monometallic shell formations, the bimetallic alloy shells were controlled to have a ca. 10 nm thickness (Figure 2d). Different from the simultaneous reduction method, the gold or silver salt could be subsequently reduced from solution by citrate in the successive reduction method forming the heterogeneous bimetallic shells on the silica spheres [28,29]. The silver and gold shells were controlled to have the thickness of ca. 5 nm, respectively, on the silica spheres, respectively. The total thickness of heterogeneous bimetallic shells hence was ca. 10 nm (Figure 2e), the same as the thickness of homogenous bimetallic alloy shells. Alternatively, the silica spheres could be subsequently deposited by the 5 nm silver at first followed by the 5 nm gold shells (Figure 2f) to achieve the heterogeneous bimetallic shells with a different geometry.

To improve the chemical stability of metal shells in solution, all monometallic and bimetallic shells were protected with the assembled monolayers of tiopronin on their external surfaces [35]. *It is also important to confirm that the metal shells were formed on the silica spheres indeed. We used hydrofluoric acid (8 vol. %) solution to dissolve the silica cores from the silica/Au shells, and the residual metal shells were cast on the copper grids for the TEM measurements (*Figure 2g). It was shown that the metal shells were clearly presented with blank spaces by the removed silica cores demonstrating the deposition of metal shells on the silica spheres.

The formation of the metal shells on the silica spheres can be well followed from the plasmon bands recorded on the ensemble absorbance spectra (Figure 3). The monometallic silver and gold shells are observed to display a single plasmon band. The silver shells have an absorbance maximum at 414 nm and the gold shells have an absorbance maximum at 538 nm in consistence to the previous reports [17–19,36,37]. The bimetallic shells exhibit their plasmon bands depending on the geometries. The homogeneous alloy shells exhibit a single plasmon band with a maximum at 494 nm (Figure 3), similar to the monometallic shells but localized between the plasmon bands of gold and silver shells [30,31]. In contrast, the heterogeneous bimetallic shells display dual plasmon bands [28,29]. The silica/Au/Ag shells have the dual absorbance maxima at 424 nm and 509 nm, and the silica/Ag/Au shells have dual absorbance maxima at 421 nm and 520 nm, respectively, which are close. It is due to different metal compositions and geometries from the metallic shells. The plasmon band from the metal nanoparticle is known to arise from the oscillations of free electrons on the metal surfaces [5,6]. For the monometallic and homogeneous bimetallic alloy shells, there is only one interface of metal-solution resulting in a single plasmon band. In contrast, for the heterogeneous bimetallic shells, there are two interfaces of metal-solution and metal-metal resulting in dual plasmon bands [26,27]. Additionally, it is noticed that the maxima of the plasmon absorption bands from the heterogeneous bimetallic shells appear primarily from their outer layer metal compositions.

To confirm these plasmon absorbance bands, a theoretical simulation method was used to study the origin of plasmon absorption bands from the metal nanoshells that have different metal components and geometries. A Finite Element Method (FEM) is used as the main theoretical analysis tool to make the simulations [36,37]. The results are presented in Figure 3b, showing that the monometallic shells display a single plasmon resonance at 430 nm for the silver shells and at 550 nm for the gold shells, approximately consistent to the plasmon bands (Ag: 414 nm and Au: 538 nm) from the experimental measurements. Like the monometallic shells, the homogeneous bimetallic alloy shell shows a single plasmon resonance at 500 nm that is also approximately consistent to the band on the actual spectrum (494 nm). It is noticed that the theoretical simulations to the heterogeneous bimetallic shells are somehow different from the measured actual spectra. The theoretical simulations show only broadened plasmon bands rather distinct dual bands as shown on the measured actual spectra. We think the differences occur because the actual heterogeneous bimetallic shells are not smooth as the theoretical metals shells in the simulations, which were also demonstrated by the TEM images. As a result, the interfaces between the metal layers should have large areas leading to significant rising of plasmon resonance bands.

We cannot rule out that the differences are due to the limitations of calculation and/or some the changing optical properties of the metal shells are small structures. But this observation is important for optimizing the near-field interactions between the fluorophores and metal shells and furthermore creating the efficient metal-enhanced fluorescence. The $Ru(bpy)_3^{2+}$ complexes were shown to have an absorbance maximum at 448 nm and an emission maximum at 613 nm (Figure 1). Because of a large Stokes shift, the $Ru(bpy)_3^{2+}$ complexes are found to have efficiently interactions with the plasmon resonances from the silver shells only in the excitation and with the plasmon resonances from the gold shells only in the emission. Consequently, we expect that the $Ru(bpy)_3^{2+}$ complexes cannot interact sufficiently with the monometallic shells on the both their excitation and emission processes. In contrast, the heterogeneous bimetallic shells display dual plasmon resonances which are approximately consistent to the excitation and emission bands of the $Ru(bpy)_3^{2+}$ complexes, and thus result in the interactions at both the excitation and emission of the $Ru(bpy)_3^{2+}$ complexes.

The emission spectra of different metal shells as well as the $Ru(bpy)_3^{2+}$-doped silica spheres were presented in Figure 4a. These spectra were normalized for two purposes. First, we intend to observe a spectral shift from the $Ru(bpy)_3^{2+}$ complexes in the silica spheres with the deposited metal shells. Second, we intend to observe the change of broadness of emission bands from the $Ru(bpy)_3^{2+}$-doped silica spheres with the deposited metal shells. The $Ru(bpy)_3^{2+}$-doped silica spheres were observed to display an emission maximum at 598 nm. With the deposition of the metal shells on the silica spheres, the emission maximum was shifted to 605 nm, 7 nm to red. The emission band was also observed to have insignificant alterations with the metal composition, implying that the $Ru(bpy)_3^{2+}$ complexes remain chemically intact in the metal shells.

The metal-enhanced fluorescence of the $Ru(bpy)_3^{2+}$ complexes in the metal shells was evaluated on both the ensemble spectral measurement and single nanoparticle imaging. First, the evaluation was performed on the ensemble spectral measurements. Typically, a typical sodium cyanide treatment was employed to remove the metal shells. Consequently, the metal-free silica spheres were released into solution [38]. Accompanying with the dissolution of metal shell by NaCN, the emission intensity on the ensemble spectra was observed to decrease progressively regarding the lost of near-field interactions. Finally, the emission spectra were decreased to minimum corresponding to complete removing of metal. The concentration of released silica sphere in solution after the treatment should be the same as the concentration of metal nanoshell prior to the treatment. The enhancement efficiency

thus could be estimated by the ratio of emission intensity of metal shell over silica sphere in the absence of metal at the same concentration in solution. The values were 4.6 folds for silica/Au shell, 6.6 folds for silica/Ag shell, 7.5 folds for silica/Ag-Au alloy shell, 14.5 folds for silica/Ag/Au shell, and 15.3 folds for silica/Au/Ag shell. The enhancement folds were presented in Figure 4b.

The emissions from the metal shells were also evaluated at the single nanoparticle level on a time-resolved confocal microscope. Typically, the metal nanoshells in solutions were diluted to nanomolar concentrations followed by casting the solutions on the glass coverslips. The emission signals were recorded on the time-resolved confocal microscope (Figure 5). In our previous report, the metal nanoparticles that were bound with a single fluorophore were also cast on the coverslip with such a highly diluted concentration. Single molecule detection (SMD) on the microscope showed clearly single-step photobleaching indicating that most metal nanoparticles were present as individuals [20]. Thus, we believe that the metal nanoshells in the current case were also presented as the single nanoparticles on the coverslips. Compared to the metal free silica spheres, the metal nanoshells are much brighter but have shorter lifetimes. For each imaging sample, at least 50 emission spots were collected to analyze its optical properties. Histogram distributions of the emission intensities from the metal nanoshells were presented in Figure 6. The optical properties of the metal free silica spheres were also determined as the control. It is shown that the silica spheres exhibit a maximum of the emission intensity at 28 counts, whereas the metal nanoshells exhibit significantly increased emission intensities. The maxima of the distribution curves for the metal shells are achieved in an order of silica/Ag/Au > silica/Au/Ag > silica/Ag-Au alloy > silica/Ag > silica/Au (Figure 6). Based on the emission intensity of the silica spheres, the enhancement factors by the metal shells could be estimated (Figure 8a), showing that both the monometallic and bimetallic shells can enhance the emission from the $Ru(bpy)_3^{2+}$ complexes doped in the silica cores.

The enhancement factors achieved on the single nanoparticle imaging method are almost completely consistent to those achieved on the ensemble spectral measurements (Figure 4b). It is shown that the bimetallic shells have larger enhancement factors than the monometallic shells. For instance, the heterogeneous bimetallic shells have an enhancement factor of 14 folds, whereas the monometallic silver nanoshells have an enhancement factor of 8.0 folds and the gold nanoshells have an enhancement of 4.3 folds significantly lower than the heterogeneous bimetallic shells. As described previously, the heterogeneous bimetallic shells exhibit double plasmon bands, and thus, can interact more efficiently with the $Ru(bpy)_3^{2+}$ complexes in the cores at the excitation and emission processes. The homogeneous bimetallic alloy shells have an enhancement factor of 9.3 folds, higher than the monometallic shells but lower than the heterogeneous bimetallic shells. It is because the homogeneous bimetallic alloy shells display a midst plasmon band between the silver and gold, and thus, have stronger interactions with the $Ru(bpy)_3^{2+}$ complexes than the monometallic shells but less than the heterogeneous bimetallic shells. It is also interesting to notice that the enhancement factor measured in ensemble solution of silica/Au/Ag is higher than that of silica/Ag/Au, however, it reverses for measurements in single nanoparticle experiments. We feel it is because of different measurement conditions for the two methods: the ensemble spectral measurements were carried out in aqueous solution whereas the single nanoparticle imaging measurements were performed under the dry condition. In addition, the enhancement factors for the two heterogeneous bimetallic shells are actually close each other within the range of measurement errors (Figure 8a).

In addition to enhanced emission intensity, the near-field interactions may bring up an increase on the intrinsic decay rate of the fluorophore, and thus, result in a significantly decreased lifetime [4,5]. The lifetime is also regarded as an important parameter to evaluate

the near-field interactions and mechanism of enhanced emission. The lifetimes of metal shells were collected in the single nanoparticle imaging measurements (Figure 5). From the histogram distributions of the lifetimes from the metal nanoshells (Figure 7), the average lifetime values were estimated as shown in Figure 8b. In this study, we collected the lifetime information from the single nanoparticle imaging. The $Ru(bpy)_3^{2+}$ complexes could not be determined at the single molecule level because of their low emission signals. In addition, the lifetime of Ru-doped silica spheres could not be also collected correctly because the lifetime was too long for the current measurement conditions. But both the lifetimes were determined previously on ensemble spectral method and used in the current system [20]. In comparison to the $Ru(bpy)_3^{2+}$-doped silica spheres, the metal nanoshells display significantly shortened lifetimes. The lifetimes of the metal shells are also shown to be different depending on the metal compositions and geometries. There is an order of reduced lifetime as silica/Au/Ag ≤ silica/Ag/Au < silica/Ag-Au alloy < silica/Ag < silica/Au, almost completely contrary to the order of increased emission intensity from the metal shells. This means that the metal shells that have largely enhanced emission intensity correspond to the metal shells that have greatly reduced lifetime regarding stronger near-field interactions between the $Ru(bpy)_3^{2+}$ complexes and metal shells. It is interesting to notice that the highest enhancement and shortest lifetimes were observed with the silica/Ag/Au structures. This result is consistent with the intuitive explanation that the internal silver shell is almost closet to the $Ru(bpy)_3^{2+}$ complexes for excitation and the gold external shells is on the outer surfaces for efficient conversation of the longer wavelength “emissive” plasmon resonance to far field radiation.

According to Jablonski Diagram of a fluorophore, the emission of an excited fluorophore is considered to consist of two energy components including fluorescence and non-radiative emission [4,5]. However, when a fluorophore is placed on a metal substrate, the near-field interaction between the fluorophore and plasmon resonance can greatly increase the fluorescence. The increased fluorescence on the metal substrate is regarded to occur on the both the excitation and emission of fluorophore [4]. The enhanced fluorescence hence includes enhanced emission at the excitation and enhanced emission at the emission. Both factors may contribute positively to the totally increased emission intensity. The contribution factors probably can be estimated from theoretical stimulations, but the treatments will be complicated. In the current system, the $Ru(bpy)_3^{2+}$ complexes are expected to interact with the silver shells principally at the excitation resulting in an enhancement of 8.0-fold and with the gold shells principally at the emission resulting in an enhancement of 4.3-fold. In the heterogeneous bimetallic shells, the near-field interactions are regarded to occur simultaneously with the silver at the excitation and with the gold at the emission processes. The total enhancement was measured to be 14-fold, larger than the factor from either of monometallic silver and gold shells. In fact, this value is close to the combination of two values, supporting our prediction that the near-field interactions on the heterogeneous bimetallic shells would be greater than those on the monometallic shells.

Conclusions

The near-field interaction can occur at both the excitation and emission of a fluorophore. For an organic fluorophore, it has a small Stoke shift so it can interact with a metal nanoparticle that has one plasmon resonance at both the excitation and emission. However, there are some large Stoke shift fluorophores such as lanthanide dyes, porphyrin derivatives, and other metal-ligand complexes that cannot interact efficiently with the single plasmon resonance from the metal nanoparticles. Thus, there is need to split one plasmon resonance from the metal nanoparticle into dual or multiple bands to couple with the excitation and emission of the fluorophore. In this study, the heterogeneous bimetallic shells were fabricated on the silica spheres and showed to have dual plasmon resonances that arise from

the metal-solution interface and metal-metal interface, respectively. The $Ru(bpy)_3^{2+}$ complexes that have a large Stokes shift was doped in the silica cores of metal shells to study the interactions between them. As controls, the monometallic and homogeneous bimetallic shells that display only one plasmon band were also generated to study the influence from the composition and geometry of metal to the near-field interactions with the fluorophores that were localized in the silica cores. The results show that the heterogeneous bimetallic shells can interact with the $Ru(bpy)_3^{2+}$ complexes more efficiently relative to the monometallic and homogeneous bimetallic shells. Our other recent research on the lanthanide-metal rod interactions showed similar effects supporting our observation in this report. On the basis of the current results, the metal plasmonics nanoparticles can be designed to contain the fluorophores with large Stokes shifts. These labeled core-shell structures may also provide a considerable promise for a novel type of metal plasmon-based fluorescence imaging agents for biological and clinical imaging applications.

Acknowledgments

The authors would like to thank support by grants from NIH (EB009509, HG-002655, HG005090, EB006521, and CA134386). We also appreciate Prof. Steve Blair from Electrical and Computer Engineering Department, University of Utah for the discussion on the theoretical simulations.

References

1. Sokolov K, Chumanov G, Cotton TM. Anal Chem. 1998; 70:3898–905. [PubMed: 9751028]
2. Ditlbacher H, Krenn JR, Felidj N, Lamprecht B, Schider G, Salerno M, Leitner A, Aussenegg FR. Appl Phys Lett. 2002; 80:404–406.
3. Jain PK, Huang X, El-Sayed IH, El-Sayed MA. Plasmonics. 2007; 2:107–118.
4. Ghosh SK, Pal T. Chem Rev. 2007; 107:4797–4862. [PubMed: 17999554]
5. Feldheim, DL.; Foss, CA. Metal Nanoparticles Synthesis, Characterization and Applications. Marcel Dekker, Inc; New York: 2002.
6. Kreibig, U.; Vollmer, M. Optical Properties of Metal Clusters. Springer-Verlag; Berlin and Heidelberg, Germany: 1995.
7. Lakowicz JR. Anal Biochem. 2005; 337:171–194. [PubMed: 15691498]
8. Lakowicz JR. Anal Biochem. 2001; 298:1–24. [PubMed: 11673890]
9. Jain PK, Huang X, El-Sayed IH, El-Sayed MA. Acc Chem Res. 2008; 41:1578–1586. [PubMed: 18447366]
10. Zhao J, Pinchuk AO, McMahon JM, Li S, Ausman LK, Atkinson AL, Schatz GC. Acc Chem Res. 2008; 41:1710–1720. [PubMed: 18712883]
11. Schwartzberg AM, Zhang JZ. J Phys Chem C. 2008; 112:10323–10337.
12. Wang H, Brandl DW, Nordlander P, Halas N. J Acc Chem Res. 2007; 40:53–62.
13. Halas NJ, Lal S, Chang W-S, Link S, Nordlander P. Chem Rev. 2011; 111:3913–3961. [PubMed: 21542636]
14. Rycenga M, Cobley CM, Zeng J, Li W, Moran CH, Zhang Q, Qin D, Xia Y. Chem Rev. 2011; 111:3669–3712. [PubMed: 21395318]
15. Lee K-S, El-Sayed MA. J Phys Chem B. 2006; 110:19220–19225. [PubMed: 17004772]
16. (a) Enderlein J. Phys Chem Chem Phys. 2004; 4:2780–2786.(b) Enderlein J. Appl Phys Letter. 2002; 80:315–317.
17. Zhang J, Fu Y, Lakowicz JR. J Phys Chem C. 2007; 111:1955–1961.
18. Zhang J, Gryczynski I, Gryczynski Z, Lakowicz JR. J Phys Chem B. 2006; 110:8986–8991. [PubMed: 16671705]
19. Zhang J, Fu Y, Lakowicz JR. J Phys Chem C. 2011; 115:7255–7260.
20. Zhang J, Fu Y, Lakowicz JR. J Phys Chem C. 2009; 113:19404–19410.
21. Xiang Y, Wu X, Liu D, Li Z, Chu W, Feng L, Zhang K, Zhou W, Xie S. Langmuir. 2008; 24:3465–3470. [PubMed: 18294010]

22. Wang X, Zhang Z, Hartland GV. J Phys Chem B. 2005; 109:20324–20330. [PubMed: 16853629]
23. Steinbrück A, Csáki A, Festag G, Fritzsche W. Plasmonics. 2006; 1:79–85.
24. Srnová-Šloufová I, Lednický F, Gemperle A, Gemperlová J. Langmuir. 2000; 16:9928–9935.
25. Ferrer D, Torres-Castro A, Gao X, Sepúlveda-Guzmán S, Ortiz-Méndez U, José-Yacamán M. Nano Lett. 2007; 7:1701–1705. [PubMed: 17497821]
26. Zhang Q, Xie J, Lee JY, Zhang J, Boothroyd C. Small. 2008; 4:1067–1071. [PubMed: 18651712]
27. Link S, Wang ZL, El-Sayed MA. J Phys Chem B. 1999; 103:3529–3533.
28. Moores A, Goettmann F. New J Chem. 2006; 30:1121–1132.
29. Ferrando R, Jellinek J, Johnston RL. Chem Rev. 2008; 108:845–910. [PubMed: 18335972]
30. Malvaldi BS, Arrighini M, Guidotti C. J Phys Chem B. 2006; 110:11050–11054. [PubMed: 16771364]
31. Belotelov VI, Carotenuto G, Nicolais L, Longo A, Pepe GP, Perlo P, Zvezdin AK. J Appl Phys. 2006; 99:044304.
32. Zhang J, Fu Y, Chowdhury M, Lakowicz JR. J Phys Chem C. 2008; 112:18–26.
33. Zhang J, Fu Y, Chowdhury M, Lakowicz JR. Nano Lett. 2007; 7:2101–2107. [PubMed: 17580926]
34. Zhang J, Lakowicz JR. J Phys Chem B. 2006; 110:2387–2392. [PubMed: 16471829]
35. Huang T, Murray RW. J Phys Chem B. 2001; 110:105, 12498–12502.
36. McMahon JM, Henry A-I, Wustholz KL, Natan MJ, Freeman RG, Van Duyne RP, Schatz GC. Anal Bioanal Chem. 2009; 394:1819–1825. [PubMed: 19305981]
37. Chowdhury MH, Gray SK, Pond J, Geddes CD, Aslan K, Lakowicz JR. J Opt Soc Am B. 2007; 24:2259–2267. [PubMed: 19777118]
38. Rosi NL, Mirkin CA. Chem Rev. 2005; 105:1547–1562. [PubMed: 15826019]

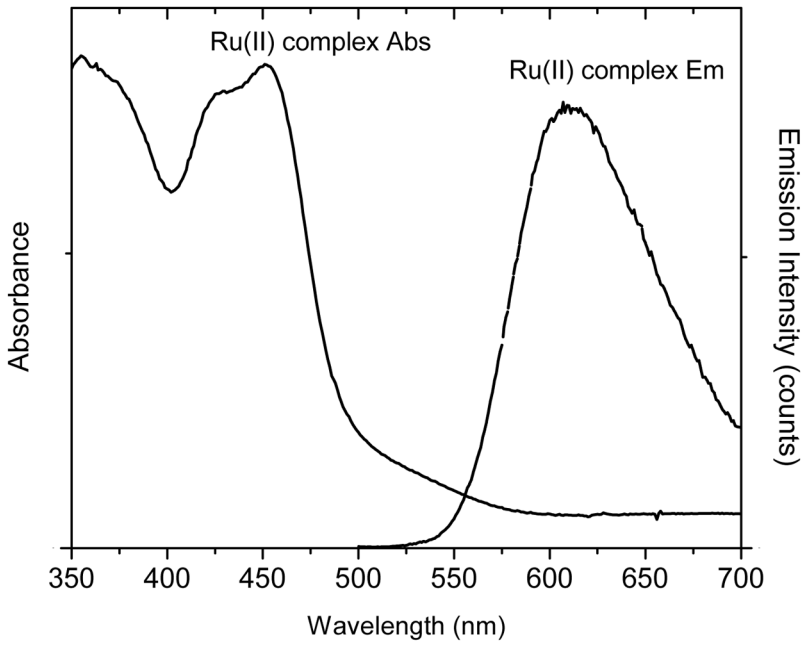

Figure 1.
Absorbance and emission spectra of $Ru(bpy)_3^{2+}$ complexes in aqueous solution upon excitation at 450 nm.

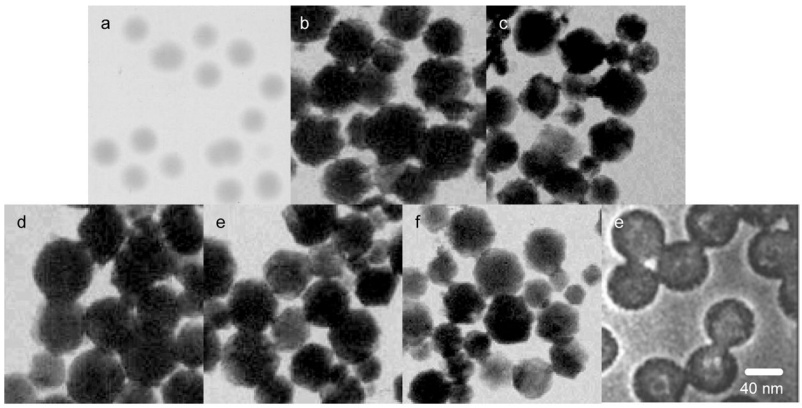

Figure 2.
TEM images for (a) silica spheres with an average 20 nm diameter, (b) monometallic silver shells on the silica spheres, (c) monometallic gold shells on the silica spheres, (d) heterogeneous bimetallic shells of silica/Ag/Au, (e) heterogeneous bimetallic shells silica/Au/Ag, (f) homogeneous bimetallic Ag-Au alloy shells on the silica spheres, and gold shells after the silica cores were removed by hydrofluoric acid.

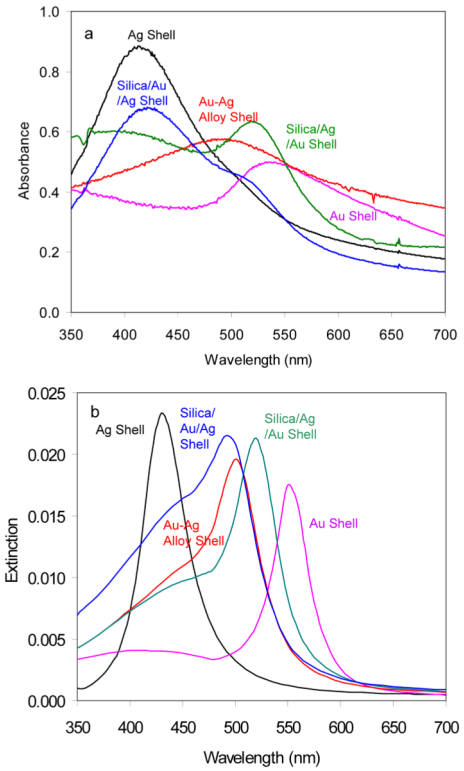

Figure 3.
(a) Measured absorption spectra of monometallic and bimetallic shells in aqueous solution and (b) theoretically simulated spectra of monometallic and bimetallic shells in aqueous solution.

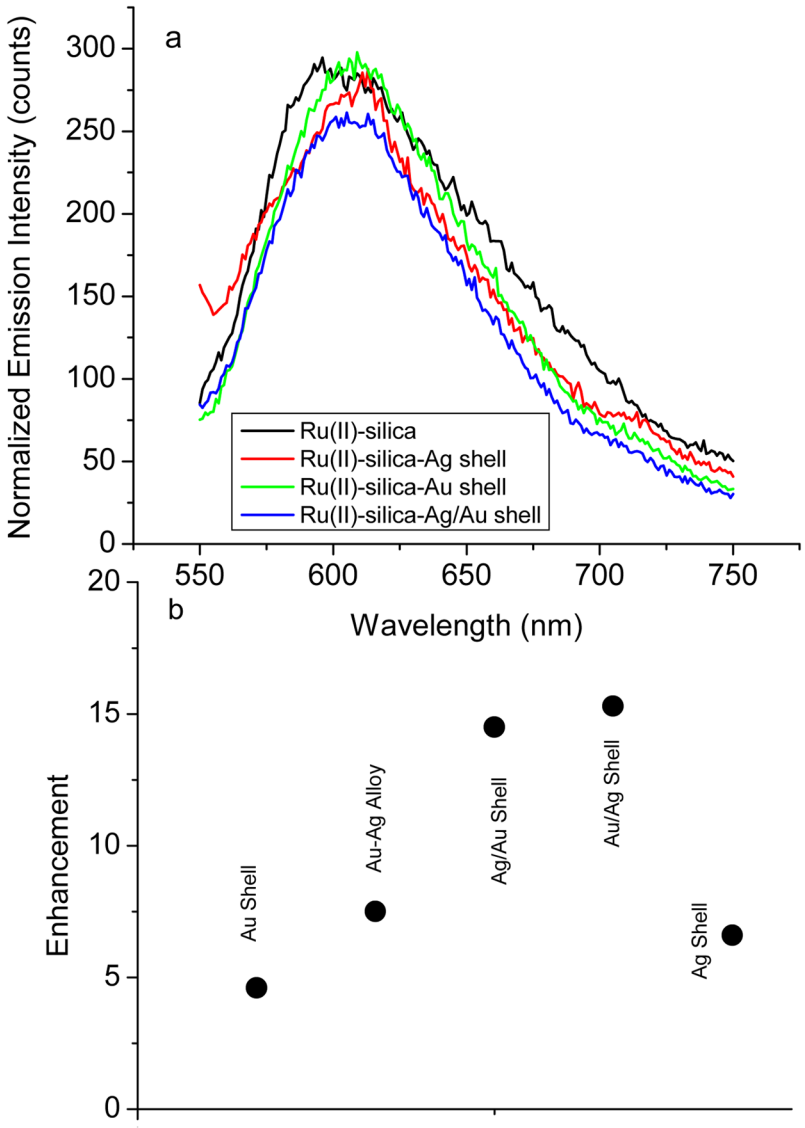

Figure 4.

(a) Measured ensemble emission spectra of $Ru(bpy)_3^{2+}$ complexes that were encapsulated in the silica spheres or in the monometallic and bimetallic nanoshells in aqueous solution upon excitation at 450 nm. (b) Enhancement folds of the $Ru(bpy)_3^{2+}$-doped metal shells obtained on the basis of ensemble spectral measurements.

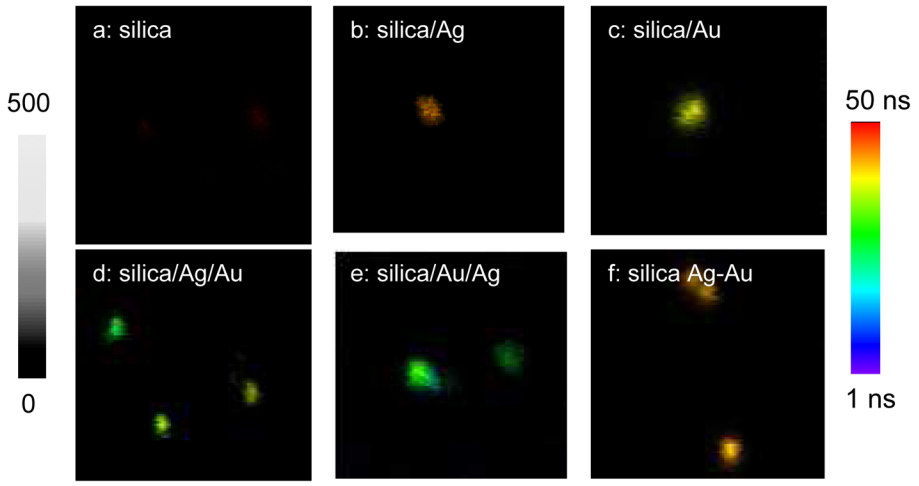

Figure 5.

Single nanoparticle images for (a) silica spheres with 20 nm diameter, (b) monometallic silver shells on the silica spheres, (c) monometallic gold shells on the silica spheres, (d) heterogeneous bimetallic shells of silica/Ag/Au on the silica spheres, (e) heterogeneous bimetallic shells of silica/Au/Ag on the silica spheres, and (f) homogeneous bimetallic Ag-Au alloy shells on the silica spheres. The images were collected upon excitation with a laser of 470 nm. The scales of the diagrams were 5 × 5 μm and the resolutions of diagrams were 100 × 100 pixel with an integration of 0.6 ms/pixel.

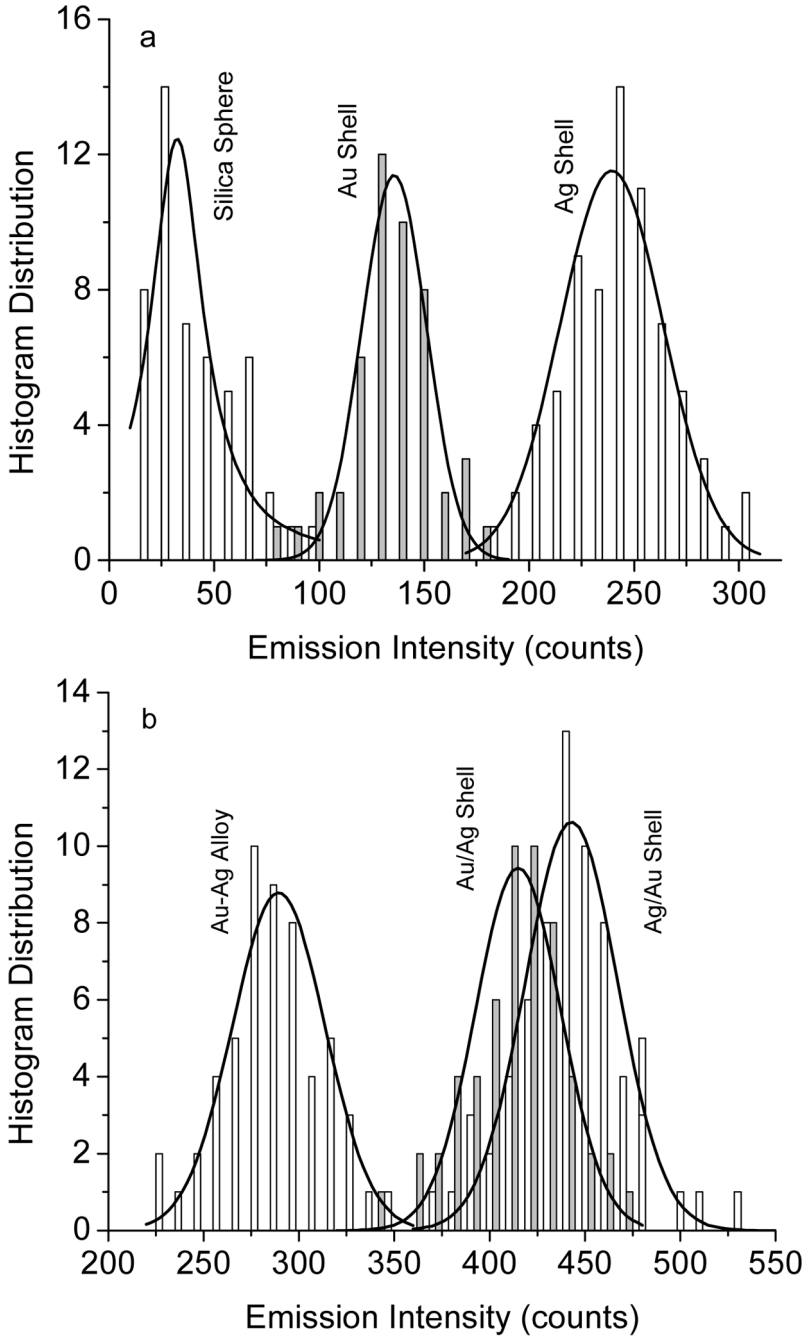

Figure 6.
Histogram distributions on the emission intensity of $Ru(bpy)_3^{2+}$ complex-encapsulated silica spheres and metal nanoshells.

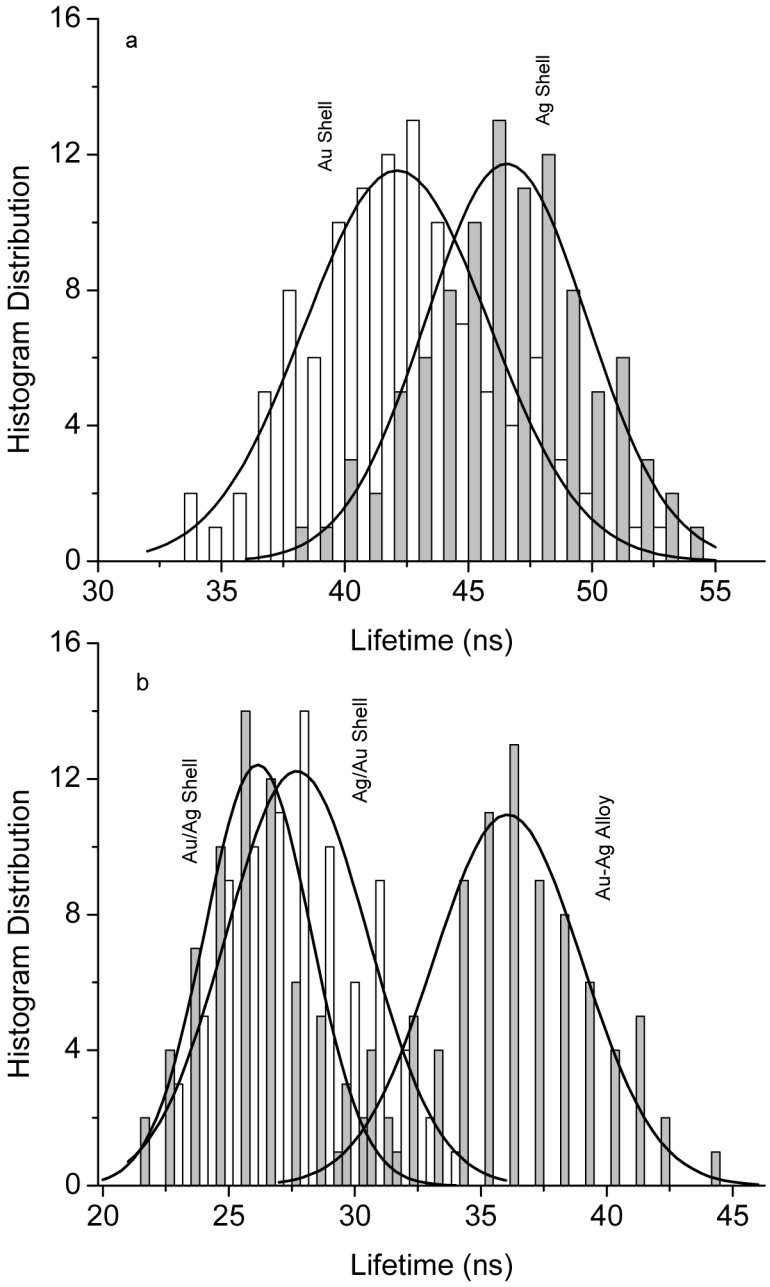

Figure 7.
Histogram distributions on the fluorescence lifetime of $Ru(bpy)_3^{2+}$ complex-encapsulated metal nanoshells..

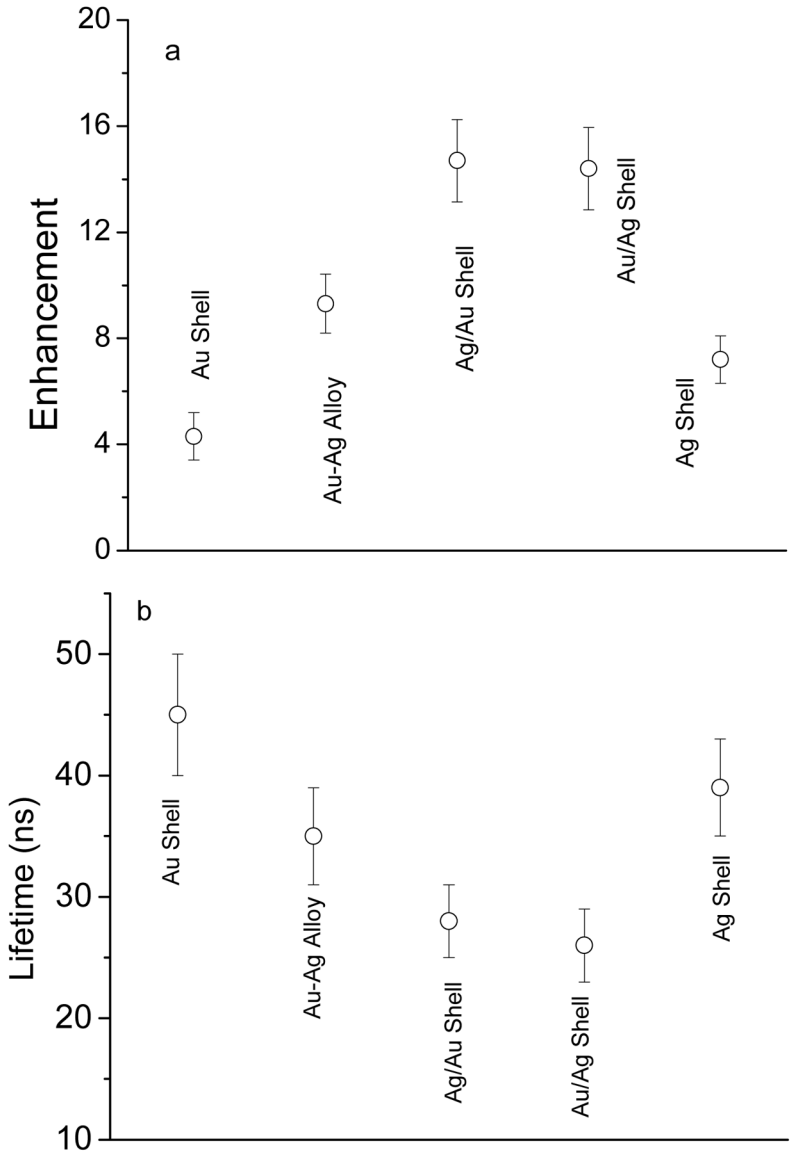

Figure 8.

(a) Enhanced emission intensity and (b) shortened lifetime of metal nanoshells. Enhancement folds on the emission intensity of metal shells were calculated on the basis of the emission intensity of metal-free silica spheres.

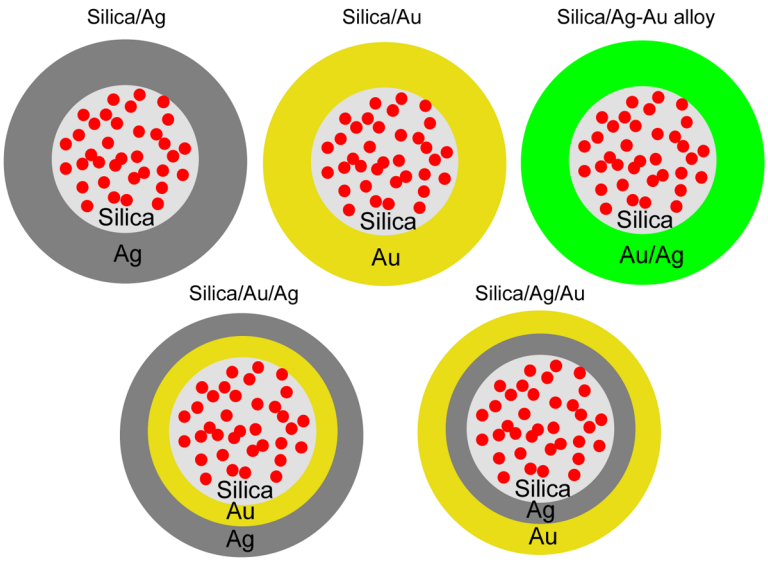

Scheme 1.

Geometries of monometallic and bimetallic shells with the $Ru(bpy)_3^{2+}$-doped silica spheres as the cores. Monometallic shells include the silver and gold shells. The bimetallic shells include the homogeneous bimetallic alloy shells and heterogeneous bimetallic shells.